Journal of ELECTRONIC MATERIALS, Vol. 48, No. 7, 2019
https://doi.org/10.1007/s11664-019-07193-8
© 2019 The Minerals, Metals & Materials Society

Structural, Chemical and Electrical Properties of Au/La_2O_3/*n*-GaN MIS Junction with a High-*k* Lanthanum Oxide Insulating Layer

M. UMA,[1] N. BALARAM,[1] P.R. SEKHAR REDDY,[2] V. JANARDHANAM,[2] V. RAJAGOPAL REDDY,[1,5] HYUNG-JOONG YUN,[3] SUNG-NAM LEE,[4] and CHEL-JONG CHOI[2,6]

1.—Department of Physics, Sri Venkateswara University, Tirupati 517 502, India. 2.—School of Semiconductor and Chemical Engineering, Semiconductor Physics Research Center (SPRC), Chonbuk National University, Jeonju 561-756, Republic of Korea. 3.—Advanced Nano Surface Research Group, Korea Basic Science Institute, Daejeon 305-806, Republic of Korea. 4.—Department of Nano-Optical Engineering, Korea Polytechnic University, Siheung 429-793, Republic of Korea. 5.—e-mail: reddy_vrg@rediffmail.com. 6.—e-mail: cjchoi@chonbuk.ac.kr

This paper demonstrates the role of high-*k* La_2O_3 on the electrical performance of the Au/*n*-GaN Schottky junction (SJ) as an insulating layer between the Au and *n*-GaN films. First, the La_2O_3 is deposited on a *n*-type GaN surface by e-beam technique and analysed for its structural and chemical properties with x-ray diffraction (XRD) and x-ray photoelectron spectroscopy (XPS) approaches. XRD and XPS results confirmed the growth of La_2O_3 on the *n*-GaN surface. Then, the Au/La_2O_3/*n*-GaN metal/insulator/semiconductor (MIS) junction is fabricated and analysed for its electrical properties and compared with the SJ electrical results. The MIS junction exhibits a good rectifying nature with a low leakage current compared to the SJ. Experimental findings reveal a higher barrier height obtained for the MIS junction than the SJ, suggesting that the barrier height is altered by the La_2O_3 insulating layer. Also, the barrier heights are estimated by Cheung's, Norde functions and Ψ_S–V plot, and the values are nearly matched with each other, indicating the techniques used here are valid. The extracted interface state density (N_{SS}) of MIS junction is lower than the SJ, implying the La_2O_3 insulating layer plays a vital role in the decreased N_{SS}. Experimental findings confirmed that the Schottky emission governs the reverse current in SJ. However, for the MIS junction, the Poole–Frenkel and Schottky emissions are the dominant current conduction mechanisms in the lower and higher bias regions.

Key words: High-*k* lanthanum oxide, *n*-type GaN, structural and chemical properties, MIS junction, electrical properties, carrier transport mechanism

INTRODUCTION

Through the past few decades, group III–V semiconductors have seen vast success due to their exciting properties such as high breakdown electric field (4.2 MV/cm), high saturation velocity ($\sim 3\times10^7$ cm/s),[1] outstanding chemical stability, and the capability to resist radiation damage.[2] Remarkably, gallium nitride (GaN) is an excellent semiconductor for the fabrication of high-temperature, high-frequency and high-power devices, which includes photodiodes, light emitting diodes (LEDs), metal/oxide/semiconductor (MOS) capacitors and electron-mobility transistors (HEMTs).[3,4] The

(Received November 23, 2018; accepted April 3, 2019; published online April 10, 2019)

conventional devices apply a Schottky barrier as the control gate which typically produces a large leakage current and, as a result, results in a decreased breakdown voltage and an enlarged power consumption as well as an extended noise coefficient.[5,6] To lower the leakage current, metal/interlayer or oxide/semiconductor (MIS/MOS) structures are proposed to update the normal Schottky gate.[4] However, the surface passivation of GaN is typically tough because of the prevailing surface defects, dangling bonds, and a few impurities, which alter the interface energy band. Hence, it is essential to research and optimize the MIS/MOS structures before fabricating the electronic devices with interlayer/oxide layer.

Various researcher groups have reported to improve barrier height and reduce leakage current in the GaN-based metal/interlayer or oxide/semiconductor (MIS/MOS) structures by using different interlayer/oxide layers.[5–18] For instance, Chiu et al.[10] prepared the Ni/AlGaN/GaN MOS-HEMTs by e-beam evaporated high-*k* La_2O_3layer as the gate insulator and reported that the gate leakage current of a metal gate GaN HEMTs was reduced one order of magnitude after inserting a La_2O_3 insulator between Ni and AlGaN. Chen et al.[11] fabricated the MIS Schottky diode hydrogen sensor with La_2O_3 as a gate insulator, and the electrical properties and gas sensing performance were examined from 25°C to 300°C. Qian et al.[12] reported the performance of La_2O_3/InAlN/GaN MOS HEMTs and found that the gate reverse leakage current was reduced by four orders of magnitude compared to the HEMTs. Jur et al.[13] demonstrated that the deposited lanthanide oxides on GaN produced stable dielectric with good interface quality. Chen et al.[14] fabricated the GaN MIS ultraviolet sensor with a La_2O_3 insulating layer, and reported a leakage current of 4.95×10^{-11} A. Chen et al.[15] studied the annealing temperature dependent electrical characteristics of La_2O_3 gate dielectric for W gated AlGaN/GaN HEMTs. Munjunath et al.[16] prepared the Au/Sm_2O_3/*n*-GaN MIS junction with a high-*k* rare-earth Sm_2O_3 as the insulating layer and found that the higher barrier height was achieved for the MIS junction compared to the Au/*n*-GaN Schottky junction. Prasad et al.[17] demonstrated the electrical and transport properties of rare-earth oxide Y_2O_3 and reported that the MIS diode showed higher barrier height compared to the conventional Au/*n*-GaN Schottky diode. Recently, Prasad et al.[18] reported the effect of annealing on the chemical, structural and electrical properties of Au/Gd_2O_3/*n*-GaN heterostructure and found that the as-deposited and 400°C annealed heterostructures showed good rectifying behaviour with very low-leakage current compared to the Au/*n*-GaN Schottky structure.

The main emphasis of the present work is to fabricate and characterize the electrical properties of an Au/La_2O_3/*n*-GaN metal/insulator/semiconductor (MIS) junction with the rare-earth high-*k* lanthanum oxide (La_2O_3) as an interlayer. Recently, the rare-earth oxides received much interest because they showed good electrical properties such as high dielectric constant and low-leakage current density.[6] Also, rare-earth oxides have attracted a significant consideration owing to new applications on passivating semiconductor interfaces.[18] For instance, Wang et al.[19,20] demonstrated a novel interface engineering technique by the insertion of *in situ* La_2O_3 between 4H-SiC and Al_2O_3 deposited in a plasma enhanced atomic layer deposition chamber, and obtained excellent interfacial and electrical characteristics by the Al_2O_3 gate dielectric with $LaSiO_x$ as the interfacial passivation layer. In this work, rare-earth lanthanum oxide (La_2O_3) is selected because of its outstanding properties such as large band gap (> 5 eV), high dielectric constant (20-30), high breakdown field (> 13 MV/cm) strength, good oxide reliability and good thermal stability.[8] Due to the low-leakage current and low interface state density of La_2O_3 thin films,[8] La_2O_3 is an excellent material for interlayer application in MIS/MOS-HEMTs. As we know, there is no complete data available yet on the barrier heights, ideality factors, series resistance and surface potential parameters of La_2O_3 films on *n*-type GaN. Certainly, it is very essential for analysing the electrical parameters which influence the device performance, consistency and steadiness. Thus, the present work mainly focuses on deposition of La_2O_3 on *n*-type GaN by e-beam evaporation and probed its structural and chemical properties with x-ray diffraction (XRD) and x-ray photoelectron spectroscopy (XPS) techniques first. Then, in order to find the role of La_2O_3 on the electrical properties of Au/*n*-GaN Schottky junction, we fabricated Au/La_2O_3/*n*-GaN MIS junctions by inserting a high-*k* rare-earth La_2O_3 insulating layer between the metal and semiconductor. The electrical parameters of the MIS junction such as barrier height, ideality factor, series resistance and interface state density are estimated with current–voltage (*I*–*V*) and capacitance–voltage (*C*–*V*) measurements. The electrical parameters of the MIS junction are correlated with the electrical results of an Au/*n*-GaN Schottky junction (SJ). Finally, a feasible current transport mechanism of SJ and MIS junctions is reviewed and discussed.

EXPERIMENTAL PROCEDURE

In this work, 2 μm-thick Si-doped GaN films ($N_d = 4.07 \times 10^{17}$ cm^{-3} by Hall measurements) were grown on c-plane sapphire substrate by the metal organic chemical vapour deposition (MOCVD) method. First, a *n*-GaN wafer was ultrasonically cleaned in warm trichloroethylene, acetone, methanol and deionized (DI) water for 5 min each step. Then, the *n*-GaN surfaces were dipped into buffered oxide etch (BOE) solution for 10 min to remove the native oxide followed by rinsing in DI water and

dried with N_2 gas. After that, the ohmic and Schottky electrodes were defined by using standard photolithography and lift-off techniques. Bilayer (Ti (30 nm)/Al (100 nm)) metals were deposited on the cleaned surface of n-GaN by the e-beam evaporation technique as the ohmic contacts were followed by a rapid thermal annealing (RTA) at 750°C for 60 s in N_2 ambient. Next, the defined contacts were dipped into BOE solution for 30 s and dried with N_2. Then, 40 nm thickness lanthanum oxide (La_2O_3) thin film was deposited on a n-GaN surface by an e-beam evaporation technique at a vacuum pressure of 7×10^{-6} Torr. Finally, 20 nm thick circular Au Schottky electrodes with a diameter of 200 μm (area = 3.14×10^{-4} cm^2) were formed on La_2O_3 thin film using an e-beam evaporation system. Now, the fabricated device type was an Au/La_2O_3/n-GaN metal/insulator/semiconductor (MIS) junction. For comparison, the Au/n-GaN Schottky junction (SJ) was made without a La_2O_3 insulating layer in the similar conditions. X-ray diffraction (XRD) technique was employed to characterize the structural properties of deposited La_2O_3 thin films. The chemical properties and depth profile of the e-beam deposited La_2O_3 thin films were carried out by x-ray photoemission spectroscopy (XPS) analysis. A precision semiconductor parameter analyzer (Agilent 4156C) and precision LCR meter (Agilent 4284A) were applied for the measurements of current–voltage (I–V) and capacitance–voltage (C–V) of the Au/n-GaN SJ and Au/La_2O_3/n-GaN MIS junctions, respectively, in the dark at room temperature.

RESULTS AND DISCUSSION

The diffraction spectrum of lanthanum oxide (La_2O_3) thin films formed by e-beam evaporation method on n-type GaN substrate is measured by the XRD technique. The XRD pattern of La_2O_3 film on n-type GaN is illustrated in Fig. 1. As seen in the XRD plot, the diffraction peaks observed at an angle '2θ' equal to 34.59° and 72.93° corresponds to the reflections from (002) and (004) planes of GaN (JCPDS no. 76-0703), respectively. The peaks obtained at 28.67°, 31.21°, 43.28°, 47.86°, 59.29°, 64.97° and 70.12° are indexed to (002), (400), (125), (600), (127), (800) and (822) planes of La_2O_3. All the peaks are assigned as per JCPDS no. 65-3185. Further, XPS measurement is employed to investigate chemical states of La_2O_3 film on n-type GaN substrate. XPS spectrum of La_2O_3 film is illustrated in Fig. 2a. As seen in XPS spectrum, the peaks are observed at 834.80 eV and 851.52 eV which can be

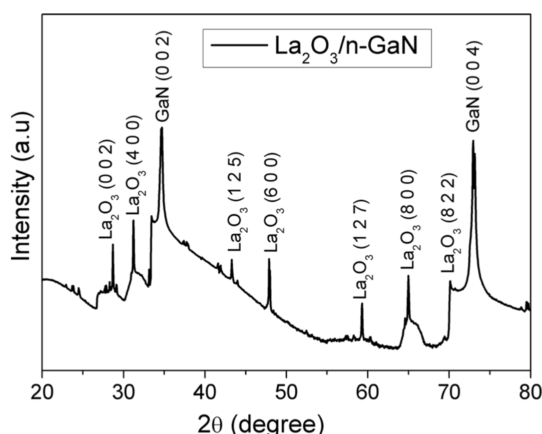

Fig. 1. X-ray diffraction spectrum of e-beam deposited La_2O_3 films on n-type GaN.

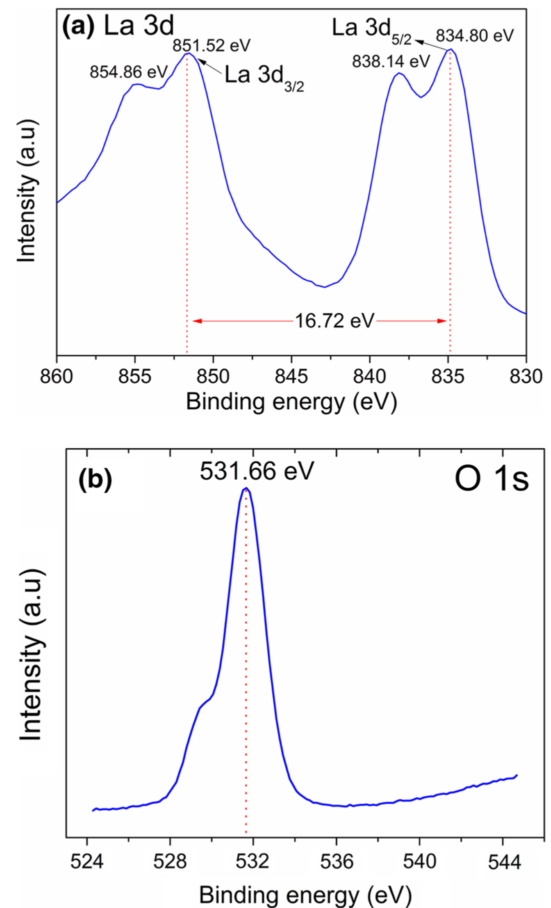

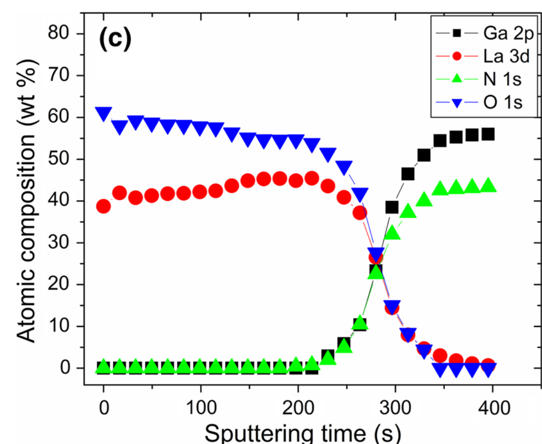

Fig. 2. XPS spectra of (a) La 3d and (b) O1s for the La_2O_3 films, and (c) XPS depth profile of the La_2O_3/n-GaN interface.

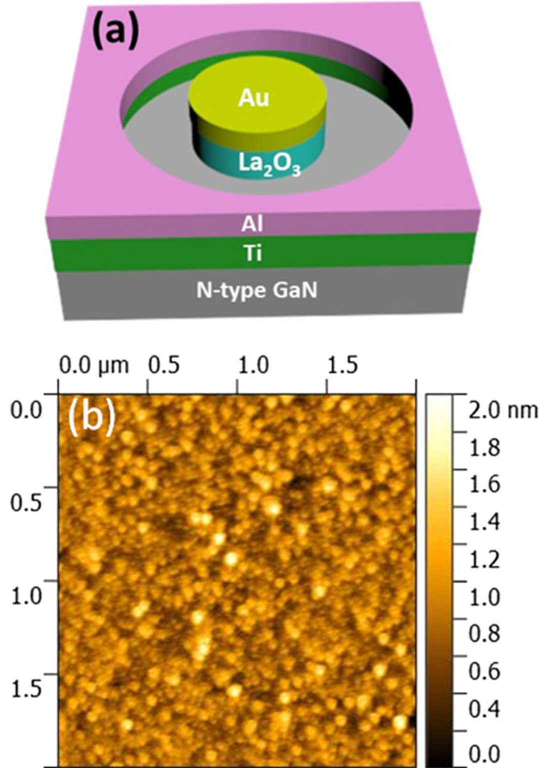

Fig. 3. (a) The schematic diagram of a fabricated Au/La_2O_3/*n*-GaN MIS junction and (b) Atomic force microscopy (AFM) image of the La_2O_3 film on *n*-type GaN.

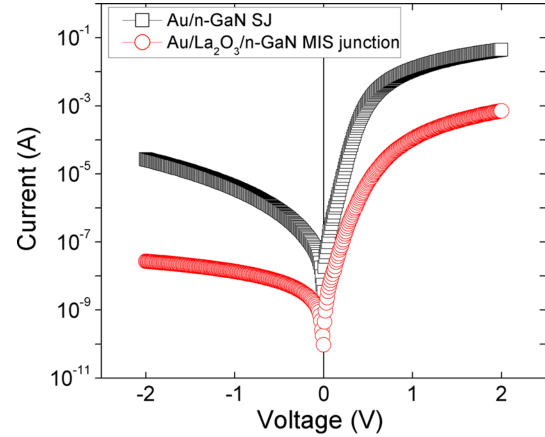

Fig. 4. Semi-logarithmic current–voltage (*I–V*) characteristics of the Au/*n*-GaN SJ and Au/La_2O_3/*n*-GaN MIS junction measured at room temperature.

attributed to two spin orbits of La $3d_{3/2}$ and La $3d_{5/2}$, respectively. The other peaks located at 854.86 eV and 838.14 eV are La 3*d* satellite peaks, indicating the presence of La^{3+}. Moreover, the spin–orbit splitting between La $3d_{3/2}$ and La $3d_{5/2}$ peaks of 16.72 eV is characteristic of La_2O_3 phase.[21,22] The binding energy of the O1*s* peak is located at 531.66 eV as shown in Fig. 2b. This peak is attributed to a La–O bond.[23] Also, the distribution of the elements across the La_2O_3/*n*-GaN layers is explored by XPS depth profile measurements. The XPS depth profile of the La_2O_3 film on *n*-type GaN is represented in Fig. 2c. As seen in Fig. 2c, the depth profile shows a sharp interface that indicates the La, O, Ga and N layers are well defined. The XRD and XPS results confirmed that the La_2O_3 film is grown on a *n*-GaN surface.

The Au/La_2O_3/*n*-GaN metal/insulator/semiconductor (MIS) junction is fabricated with a La_2O_3 as an insulating layer between the Au and *n*-GaN layers to associate with the structural and chemical properties of La_2O_3 thin films. The schematic diagram of a fabricated Au/La_2O_3/*n*-GaN MIS junction with a high-*k* rare-earth La_2O_3 insulating layer is shown in Fig. 3a. Figure 3b shows the atomic force microscopy (AFM) image of the e-beam deposited La_2O_3 thin film on *n*-GaN. The surface morphology of the La_2O_3 thin films is considerably smooth with a root-mean-square (rms) roughness of 1.022 nm.

Figure 4 depicts the semi-logarithmic reverse and forward *I–V* characteristics of a SJ and MIS junction measured at room temperature. It is noted that both the SJ and MIS junction shows a good rectifying nature with the rectification ratio of 1×10^3 and 2×10^4, respectively. The rectification ratio of the MIS junction is higher by one order than the SJ. The reverse leakage current is found to be 3.93×10^{-6} A and 1.35×10^{-8} A at -1 V for the SJ and MIS junction. It is noted that the measured reverse leakage current of the MIS junction decreases by two orders of magnitude than the SJ, implying the La_2O_3 insulating layer plays an important role in the reduction of reverse leakage current. This indicates that the electrical properties of the MIS junction are improved as compared to the SJ. Also, non-saturation behaviour is observed as a function of applied bias voltage in the reverse bias for the both SJ and MIS junctions. This can be attributed to the image force lowering of barrier height (BH) and the existence of a native oxide or deposited insulating layer at the metal/semiconductor junction.[24,25] The series resistance (R_S) and shunt resistance (R_{SH}) are also extracted from the *I–V* characteristics, and the corresponding values are 26 Ω and 655 kΩ for SJ, and 735 Ω and 27 MΩ for the MIS junction. These results reveal that the junction with and without insulating layer has low R_S and high R_{SH}. The derived values of R_S and R_{SH} are appropriate for the fabrication of SJ and MIS type Schottky diodes or electronic devices.[25] The forward *I–V* characteristics of SJ and MIS junctions are analyzed using the thermionic emission (TE) theory.[26] The BH and *n* values are found to be 0.67 eV, 1.35 and 0.78 eV, 1.72 for SJ and MIS junctions, respectively. Clearly, it is seen that the BH of the MIS junction increases compared to the SJ junction after inclusive of a La_2O_3 thin insulating layer. This may be due to the physical barrier formed by a La_2O_3 insulating layer between the Au and *n*-GaN films. Consequently, the insulating layer makes an excess BH of 0.11 eV which indicates the

La_2O_3 insulating layer enhances the BH of SJ. It is noted that the estimated ideality factor of SJ and MIS junction deviated from unity indicating the non-ideal behaviour of the device. This may be attributed to interface states at a native thin oxide layer between metal and semiconductor, electron tunnelling through the barrier, charge carrier recombination in depletion region and generation–recombination through interface traps in the junction.[27] Another reason may be the existence of a wide distribution of low Schottky barrier patches produced by a laterally inhomogeneous barrier.[25]

The Au/n-GaN SJ and Au/La_2O_3/n-GaN MIS junction shows a non-linear region in the forward bias I–V curves at higher voltage region (Fig. 4). This can be because of the effect of series resistance (R_S) and interface state density (N_{SS}). However, the BH and ideality factor are significant in linear and non-linear regions of the I–V characteristics. In order to estimate BH, ideality factor (n) and series resistance (R_S) of the SJ and MIS junction in a non-linear region of the forward bias I–V characteristics, Cheung's functions were employed.[28] Cheung's functions can be expressed as

$$\frac{\mathrm{d}V}{\mathrm{d}(\ln I)} = \frac{nkT}{q} + IR_S, \tag{1}$$

$$\mathrm{H}(I) = V - \left(\frac{nkT}{q}\right)\ln\left(\frac{I}{AA^{*}T^{2}}\right), \tag{2}$$

and

$$\mathrm{H}(I) = n\Phi_b + IR_S. \tag{3}$$

Figure 5a and b demonstrate the dV/d(ln$I$) versus I, and H(I) versus I plots for the Au/n-GaN SJ and Au/La_2O_3/n-GaN MIS junction. Using the dV/d(ln$I$)-I plot (Fig. 5a and b), the R_S and n values are determined to be 39 Ω and 1.9 for the SJ, and 11 kΩ and 2.0 for the MIS junction, respectively. Whereas, the BH and R_S are determined to be 37 Ω and 0.65 eV for the SJ, and 10 kΩ and 0.75 eV for the MIS junction, respectively from the H(I)-I plot (Fig. 5a and b). The R_S values extracted from the dV/d(ln$I$) versus I and H(I) versus I are closely matched with one another, indicating the Cheung's functions are consistent and valid. It is noticed that the estimated R_S of the MIS junction is somewhat higher than the SJ, implying that the interfacial insulating layer exists at the interface. The ideality factor derived from the linear region of I–V and dV/d(ln$I$)–I plot is slightly different from each other, this can be associated with the effect of series resistance and the bias dependence of BH along with the voltage drop across the interfacial layer and the change of interface states with bias in the non-linear region of the I–V characteristics.[29–31] Moreover, the BH and R_S of the SJ and MIS junction are estimated by employing the modified

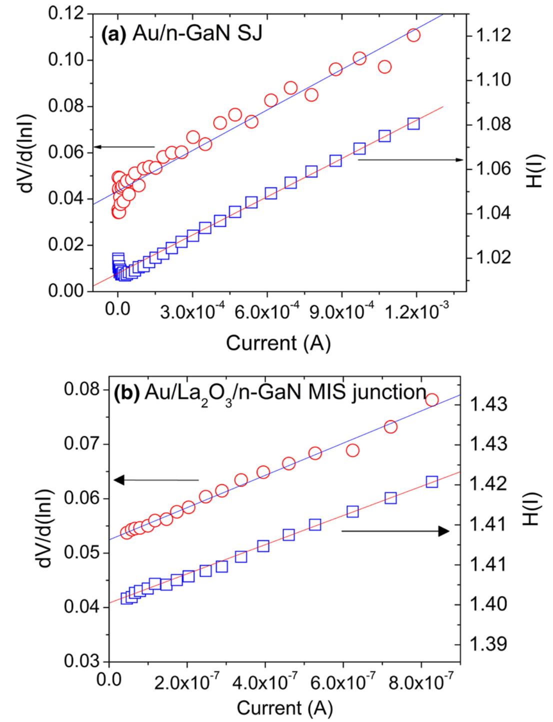

Fig. 5. (a) dV/d(ln$I$) versus I and H(I) versus I plot for the Au/n-GaN SJ, and (b) dV/d(ln$I$) versus I and H(I) versus I plot for the Au/La_2O_3/n-GaN MIS junction.

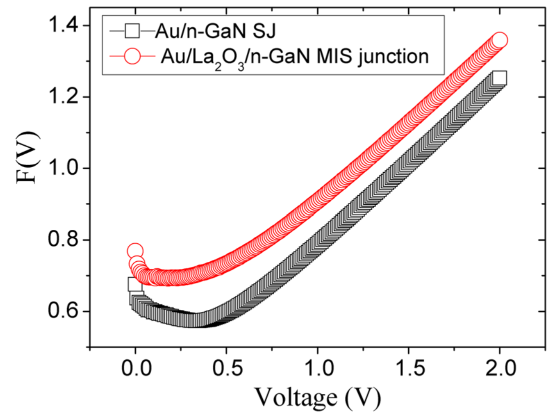

Fig. 6. Plot of F(V) versus V for the Au/n-GaN SJ and Au/La_2O_3/n-GaN MIS junction.

Norde function.[32] Figure 6 illustrates the Norde function $F(V)$ against voltage (V) plot for the Au/n-GaN SJ and Au/La_2O_3/n-GaN MIS junction. Using this plot, the BH and R_S are determined to be 0.69 eV and 5 kΩ, and 0.75 eV and 10 kΩ for the SJ and MIS junction, respectively.

In addition, when the metal comes into contact with a semiconductor, the current through a junction with a native oxide layer on the surface of the semiconductor is expressed by

$$I = AA^{*}T^{2}\exp\left(-\frac{q\Psi_S}{kT}\right)\left[\exp\left(-\frac{qV_n}{nkT}\right)\right], \tag{4}$$

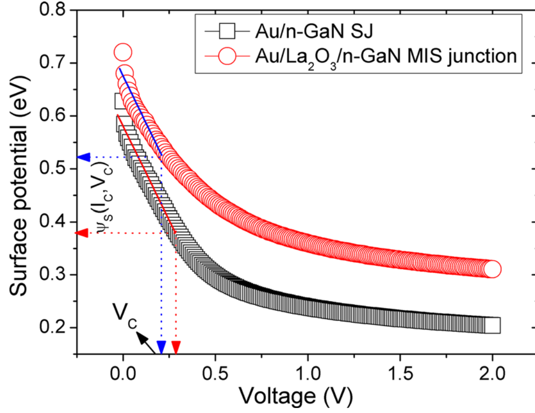

Fig. 7. Ψ_S versus V plot of the Au/*n*-GaN SJ and Au/La_2O_3/*n*-GaN MIS junction.

where A, A^*, T, k, and n have their usual meanings.[31] The surface potential, Ψ_S, is given by

$$\psi_s = \frac{kT}{q}\ln\left(\frac{AA^*T^2}{I}\right) - V_n, \tag{5}$$

where V_n is the potential difference between the Fermi level and the valence band maximum and $V_n = (kT/q)\ \ln\ (N_c/N_d)$, where N_c is the effective density of states in the conduction band and N_d is the carrier concentration and then V_n can be extracted. With the help of Eq. 5, Ψ_S is derived by substituting the value of V_n. The derived Ψ_S values against the forward voltage (V) are depicted in Fig. 7. By using Ψ_S–V plot, the critical potential, Ψ_S (I_C,V_C), and critical voltage (V_C) are achieved. Then, the BH can be calculated by the following equation and it is defined as[33]

$$\Phi_b = \Psi_S(I_C, V_C) + C_2V_C + V_n. \tag{6}$$

As seen in Fig. 7, the Ψ_S value decreases linearly up to V reaching the critical value V_C. Also, C_2 is the inverse of the ideality factor and is expressed by

$$-C_2 = \left(\frac{d_s}{dV}\right)_{I_C,V_C} = \frac{1}{n}. \tag{7}$$

The BH and ideality factor values are estimated using Eqs. 6 and 7 and the corresponding values are 0.64 eV and 1.35, and 0.74 eV and 1.42 for the SJ and MIS junction, respectively. The BHs estimated from the I–V, Cheung's, Norde functions and Ψ_S–V plot are nearly similar; hence, the methods applied here are consistent and effective.

Figure 8 demonstrates the $1/C^2$ characteristics of the Au/*n*-GaN SJ and Au/La_2O_3/*n*-GaN MIS junction measured at a frequency of 1 MHz, showing linear behaviour. Therefore, the depletion layer capacitance can be expressed by[22]

$$\frac{1}{C^2} = \left(\frac{2}{\varepsilon_s q N_d A^2}\right)\left(V_{bi} - \frac{kT}{q} - V\right), \tag{8}$$

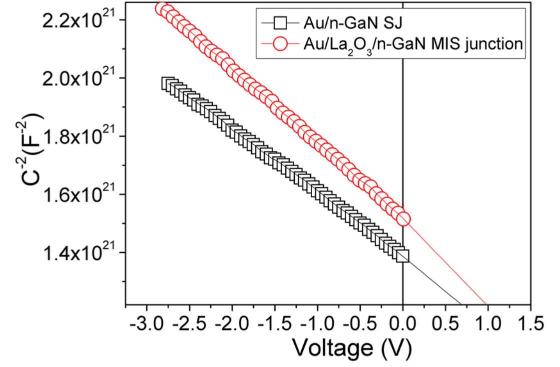

Fig. 8. Plot of C^{-2} versus V for the Au/*n*-GaN SJ and Au/La_2O_3/*n*-GaN MIS junction.

where ε_s, q, N_d, k, T, V and A have the usual meanings.[17] V_{bi} is the built-in potential which is given by the equation $V_{bi} = V_o + kT/q$, here V_o is estimated from the x-intercept of the plot of $1/C^2$ versus V. Then, the BH can be estimated by the equation $\Phi_b = V_o + V_n + kT/q$, here $V_n = (kT/q)\ln(N_C/N_d)$ and the density of states in the conduction band edge is given by $N_C = 2(2\pi m^*kT/h^2)^{3/2}$. The built-in potential values are determined to be 0.70 V and 0.89 V for the MS and MIS junction, respectively. Then, the barrier heights are estimated to be 0.95 eV for SJ and 1.15 eV for the MIS junction. The BHs estimated by the C–V approach are larger than the values by way of the I–V approach; this could be because of the specific nature of C–V and I–V techniques. Other reasons may be the presence of excess capacitance, the BHs are different. The BHs are differing from C–V and I–V techniques and that may be because of the effect of the image force lowering and the barrier inhomogeneities.[34] Other reasons may be because of the defects in the interface, overruling insulating layer edge leakage current and deep impurity levels.[35] The estimated BHs, ideality factors and series resistance by I–V, Cheung's, Ψ_S–V plot and C–V approaches are summarized in Table I. Some of the reported barrier height values of Au/*n*-GaN SJ and GaN-based MIS/MOS type devices are also given in Table I for comparison.

Furthermore, the electrical characteristics of the SJ and MIS junction are departing from ideality because of the interface state density, voltage dependent ideality factor ($n(V)$) and effective BH (Φ_e) and the presence of an insulating layer. As proposed by Card and Rhoderick,[40] the interface state density (N_{SS}) is expressed by

$$N_{SS}(V) = \frac{1}{q}\left[\frac{\varepsilon_i}{\delta}(n(V) - 1) - \frac{\varepsilon_s}{W_d}\right], \tag{9}$$

$$\text{here}\quad n(V) = \frac{qV}{kT\ln\left(^{I}/_{I_o}\right)}, \tag{10}$$

Table I. The estimated barrier height, ideality factor and series resistance of the Au/*n*-GaN SJ and Au/La_2O_3/*n*-GaN MIS junction. Some of the reported barrier height values of the Au/*n*-GaN and GaN-based MIS/MOS type devices are given for comparison

Parameters	Au/*n*-GaN MS	Au/La_2O_3/*n*-GaN MIS junction	Reported Φ_b (eV) values from the literature
I–V method			
Barrier height, Φ_b (eV)	0.67	0.76	Present work
Ideality factor (n)	1.35	1.72	0.73 eV,[36] 0.71 eV,[37] 0.65 eV,[38] 0.73 eV and 0.94 eV,[39] 0.68 eV and 0.81 eV,[16] 0.71 eV and 0.98 eV,[18] 0.69 eV and 0.82 eV,[25] 0.70 eV and 0.89 eV[31]
Cheung's method			
dV/d(ln$I$) versus I			
Series resistance (Ω)	39	11 k	
Ideality factor (n)	1.9	2.0	
H (I) versus I			
Barrier height, Φ_b (eV)	0.65	0.75	
Series resistance (Ω)	37	10 k	
Norde method			
Barrier height, Φ_b (eV)	0.71	0.75	
Series resistance (Ω)	5 k	10 k	
Surface potential			
Barrier height Φ_b (eV)	0.64	0.74	
Ideality factor (n)	1.23	1.39	
C–V method			
Built-in potential (V)	0.70	0.95	
Barrier height, Φ_b (eV)	0.89	1.15	
Interface state density (N_{SS}) (eV^{-1} cm^{-2})	7.15×10^{13} to 1.50×10^{13}	1.36×10^{13} to 2.85×10^{12}	

where ε_i and ε_s are permittivity of the interlayer and semiconductor, respectively, δ is the thickness of the interfacial layer and W_d is the depletion width which is extracted by high frequency (1 MHz) *C–V* data. The energy of interface states (E_{SS}) are extracted with respect to the conduction band at the semiconductor surface (E_C) for n-type semiconductors and is expressed by the following relation

$$E_C - E_{SS} = q(\Phi_e - V),\quad \text{where } \Phi_e = \Phi_{bo} + \beta V = \Phi_{bo} + \left(1 - \frac{1}{n(V)}\right)V. \tag{11}$$

Figure 9 depicts the N_{SS} versus E_C-E_{SS} plot for the SJ and MIS junction. As seen in Fig. 9, the N_{SS} increases exponentially from the mid gap towards the bottom of the conduction band. The determined N_{SS} values are varied from 1.50×10^{13} eV cm^{-2} to 7.15×10^{13} eV cm^{-2} for the SJ and 2.85×10^{12} eV cm^{-2} to 1.36×10^{13} eV cm^{-2} for the MIS junction, respectively. It is observed that the estimated N_{SS} of the MIS junction is less than the SJ, indicating that the GaN surface is efficiently passivated by the La_2O_3 insulating layer. These results suggest that the La_2O_3 insulating layer plays a vital role in reducing N_{SS} and enhances the effective BH of the SJ.

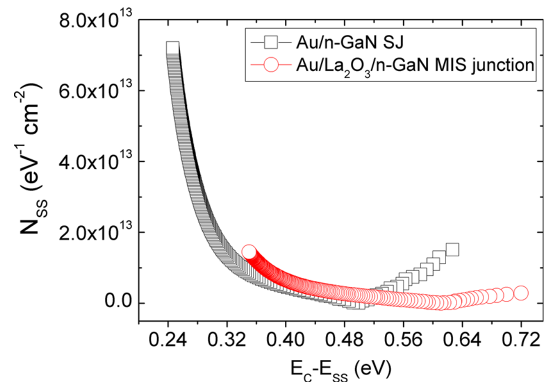

Fig. 9. Plot of N_{SS} versus E_C-E_{SS} for the Au/*n*-GaN SJ and Au/La_2O_3/*n*-GaN MIS junction.

In order to know the reverse current conduction mechanism in the Au/*n*-GaN SJ and Au/La_2O_3/*n*-GaN MIS junction, the reverse current ln(I_R) versus voltage $(V_R)^{1/2}$ plot is drawn and is illustrated in Fig. 10. The reverse current is associated with the Poole–Frenkel emission (PFE) and is expressed as[41]

$$I_R = I_0 \exp\left(\frac{S_{PFE} V^{1/2}}{kTd^{1/2}}\right), \quad (12)$$

and for Schottky emission

$$I_R = AA^* T^2 \exp\left(\frac{-\Phi_b}{kT}\right) \exp\left(\frac{S_{SE} V^{1/2}}{kTd^{1/2}}\right), \quad (13)$$

where d is the thickness of the film, S_{PFE} and S_{SE} are the Poole–Frenkel and Schottky field lowering coefficients, respectively. The theoretical values of S_{PFE} and S_{SE} are estimated by

$$S_{PFE} = 2S_{SE} = \left(\frac{q^3}{\pi \varepsilon_s \varepsilon_0}\right)^{1/2}, \quad (14)$$

here q, ε_s and ε_o are the electric charge, relative permittivity of the semiconductor and the free space. Always, the S_{PFE} value is twice the value of the S_{SE}. The S_{PFE} and S_{SE} values are calculated theoretically using the Eq. 14 by substituting the values of ε_s and ε_o and the values are 2.46×10^{-5} eV m$^{1/2}$ V$^{-1/2}$ and 1.23×10^{-5} eV m$^{1/2}$ V$^{-1/2}$ for the SJ, and 1.46×10^{-5} eV m$^{1/2}$ V$^{-1/2}$ and 0.73×10^{-5} eV m$^{1/2}$ V$^{-1/2}$ for the MIS junction, respectively. From Fig. 10, the extracted slope value is 0.49×10^{-5} eV m$^{1/2}$ V$^{-1/2}$ for the SJ which is almost matched with the theoretical value of the S_{SE}. Hence, the reverse leakage current conduction mechanism is governed by Schottky emission in SJ. However, in the case of the MIS junction, there are two distinct regions observed (Fig. 10) that show the two different conduction mechanisms that occur in the reverse bias. The extracted slope values are 2.40×10^{-5} eV m$^{1/2}$ V$^{-1/2}$ in the lower bias region (region I), and 1.05×10^{-5} eV m$^{1/2}$ V$^{-1/2}$ in the higher bias region (region II) for the MIS junction. The extracted slope value in region I is found to be nearly matched with the theoretical value of Poole–Frenkel lowering coefficients. Hence, the reverse leakage current conduction mechanism is dominated by the Poole–Frenkel emission in region I. This indicates that the carrier transport occurs from the metal into conductive dislocations through traps states than through straight emission from the metal.[41,42] However, the extracted slope value in the region II is nearly matched with the theoretical value of Schottky lowering coefficients. This suggests that the Schottky emission is the dominant current conduction mechanism in the region II where current conduction takes place through the interface rather than from bulk material. This is due to the sub-atomic structure and non-uniformity of the dielectric layer employed here.[43,44]

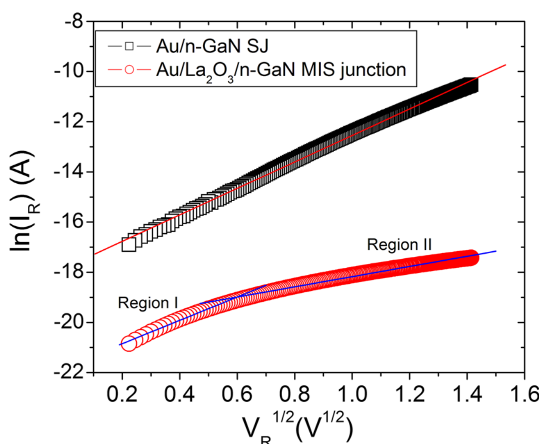

Fig. 10. Plot of ln(I_R) versus $V_R^{1/2}$ for the Au/n-GaN SJ and Au/La_2O_3/n-GaN MIS junction.

CONCLUSIONS

In order to understand the effect of the La_2O_3 insulating layer on the electrical parameters of Au/n-GaN SJ, the Au/La_2O_3/n-GaN MIS junction is developed by a place for La_2O_3 between the Au and n-GaN semiconductor. First, the La_2O_3 thin film is formed by the e-beam evaporation approach on a n-type GaN surface and explored for its structural and chemical properties using XRD and XPS measurements. The results of XRD and XPS indicate that the La_2O_3 film is formed on the n-GaN surface. The electrical performance of the SJ and MIS junction are measured by I–V and C–V approaches at room temperature. The electrical parameters of the Au/La_2O_3/n-GaN MIS junction are correlated with the results of Au/n-GaN SJ. The MIS junction showed an excellent rectifying behaviour with a low reverse leakage current compared to the SJ. Results showed that a higher barrier height is obtained for the MIS junction (0.76 eV (I–V)/0.95 eV (C–V)) than the SJ (0.67 eV (I–V)/0.70 eV (C–V)). Using Cheung's, Norde functions and Ψ_S–V plot, the barrier heights are derived for the SJ and MIS junction, and it is found that the values are almost matched with one another, suggesting that the methods applied here are dependable and effective. The estimated interface state density (N_{SS}) of the MIS junction is lower than the SJ, implying the La_2O_3 insulating layer participated in the reduction of N_{SS}. Observations revealed that the Schottky emission is the dominant current conduction mechanism in the reverse bias of SJ. However, in the case of the MIS junction, the Poole–Frenkel emission is dominant in the lower bias region, whereas the Schottky emission is dominant in the higher bias region. Experimental findings suggested that La_2O_3 films can be a desirable dielectric material in the development of MIS/MOS devices.

ACKNOWLEDGMENTS

This work was supported by the National Research Foundation of Korea (NRF) grant (NRF-2017R1A2B2003365) funded by the Ministry of Education, Republic of Korea, and by the Transfer machine specialized lighting core technology development professional manpower training project

(Project No. N0001363) funded by the Ministry of Trade, Industry and Energy, Republic of Korea.

REFERENCES

1. M. Zheng, G. Zhang, X. Wang, J. Wan, H. Wu, and C. Liu, *Nanoscale Res. Lett.* 12, 267 (2017).
2. W. Saito, Y. Takada, M. Kuraguchi, K. Tsuda, I. Omura, T. Ogura, and H. Ohashi, *IEEE Trans. Electron Devices* 50, 2528 (2003).
3. T. Kachi, *Jpn. J. Appl. Phys.* 53, 100210 (2014).
4. J.W. Chung, J.C. Roberts, E.L. Piner, and T. Palacios, *IEEE Electron Device Lett.* 29, 1196 (2008).
5. S.W. Kang and S.W. Rhee, *J. Electrochem. Soc.* 149, C345 (2002).
6. S.S. Ohmi, C. Kobayashi, I. Kashiwagi, C. Ohshima, H. Ishiwara, and H. Iwai, *J. Electrochem. Soc.* 150, F134 (2003).
7. Y. Kim, S. Ohmi, K. Tsutsui, and H. Iwai, *Jpn. J. Appl. Phys.* 44, 4032 (2005).
8. F.C. Chiu, H.W. Chou, and J.Y. Lee, *J. Appl. Phys.* 97, 103503 (2005).
9. C.H. Hsu, M.T. Wang, and J.Y. Lee, *J. Appl. Phys.* 100, 074108 (2006).
10. H.C. Chiu, C.W. Lin, C.H. Chen, C.W. Yang, C.K. Lin, J.S. Fu, L.B. Chang, R.M. Lin, and K.P. Hsueh, *J. Electrochem. Soc.* 157, H160 (2010).
11. G. Chen, J. Yu, and P.T. Lai, *Microelectron. Reliab.* 52, 1660 (2012).
12. F. Qian, L. Qian, X. Tao, W. Qiang, Z. Jin-Cheng, and H. Yue, *Chin. Phys. B* 21, 067305 (2012).
13. J.S. Jur, V.D. Wheeler, D.J. Lichtenwalner, J.P. Maria, and M.A.L. Johnson, *Appl. Phys. Lett.* 98, 042902 (2011).
14. P.C. Chen, C.H. Chen, C.M. Tsai, C.F. Cheng, and S.L. Wu, *Surf. Coat. Technol.* 231, 328 (2013).
15. J. Chen, T. Kawanago, H. Wakabayashi, K. Tsutsui, H. Iwai, D. Nohata, H. Nohira, and K. Kakushima, *Microelectron. Reliab.* 60, 16 (2016).
16. V. Manjunath, V. Rajagopal Reddy, P.R. Sekhar Reddy, V. Janardhanam, and C.J. Choi, *Curr. Appl. Phys.* 17, 980 (2017).
17. C. Venkata Prasad, V. Rajagopal Reddy, and C.J. Choi, *Appl. Phys. A* 123, 279 (2017).
18. C. Venkata Prasad, M. Siva Pratap Reddy, V. Rajagopal Reddy, and C. Park, *Appl. Surf. Sci.* 427, 670 (2018).
19. Q. Wang, X. Cheng, L. Zheng, P. Ye, M. Li, L. Shen, J. Li, D. Zhang, Z. Gu, and Y. Yu, *Appl. Surf. Sci.* 410, 326 (2017).
20. Q. Wang, X. Cheng, L. Zheng, L. Shen, D. Zhang, Z. Gu, R. Qian, D. Cao, and Y. Yu, *Appl. Surf. Sci.* 428, 1 (2018).
21. T. Honma, Y. Benino, T. Fujiwara, T. Komatsu, R. Sato, and V. Dimitrov, *J. Appl. Phys.* 91, 2942 (2002).
22. C. Yang, H. Fan, S. Qiu, Y. Xi, and Y. Fu, *J. Non-Cryst. Solids* 355, 33 (2009).
23. Y. Li, B. Guan, A. Maclennan, Y. Hu, D. Li, J. Zhao, Y. Wang, and H. Zhang, *Electrochim. Acta* 241, 395 (2017).
24. E.H. Rhoderick and R.H. Williams, *Metal-Semiconductor Contacts*, 2nd ed. (Oxford: Clarendon, 1988).
25. V. Rajagopal Reddy, V. Janardhanam, J. Won, and C.J. Choi, *J. Colloid Interface Sci.* 499, 180 (2017).
26. S.M. Sze and K.K. Ng, *Physics of Semiconductors Devices*, 3rd ed. (New Jersey: Wiley, 2007).
27. M. Das, J. Datta, R. Jana, S. Sil, S. Halder, and P.P. Ray, *New J. Chem.* 41, 5476 (2017).
28. S.K. Cheung and N.W. Cheung, *Appl. Phys. Lett.* 49, 85 (1986).
29. P. Prabhu Thapaswini, R. Padma, N. Balaram, B. Bindu, and V. Rajagopal Reddy, *Superlatt. Microstruct.* 93, 82 (2016).
30. S. Karatas, S. Altindal, A. Turut, and M. Cakar, *Phys. B* 392, 43 (2007).
31. V. Rajagopal Reddy, P.R. Sekhar Reddy, I. Neelakanta Reddy, and C.J. Choi, *RSC Adv.* 6, 105761 (2016).
32. H. Norde, *J. Appl. Phys.* 50, 5052 (1979).
33. P. Chattopadhyay, *Solid State Electron.* 38, 739 (1995).
34. V. Rajagopal Reddy, D. Sri Silpa, V. Janardhanam, H.J. Yun, and C.J. Choi, *Electron. Mater. Lett.* 11, 73 (2015).
35. S.M. Sze, *Physics of Semiconductor Devices*, 2nd ed. (New York: Wiley, 1981).
36. B. Deb, A. Ganguly, S. Chaudhuri, B.R. Chakraborti, and A.K. Pal, *Mater. Chem. Phys.* 74, 282 (2002).
37. M. Diale and F.D. Auret, *Phys. B* 404, 4415 (2009).
38. R. Khelifi, H. Mazari, S. Mansouri, Z. Benamara, M. Mostefaoui, K. Ameur, N. Benseddik, P. Marie, P. Ruterana, I. Monnet, J.M. Bluet, and C. Bru-Chevallier, *Sens. Transd.* 27, 217 (2014).
39. V. Rajagopal Reddy and C. Venkata Prasad, *Mater. Sci. Eng. B* 231, 74 (2018).
40. H.C. Card and E.H. Rhoderick, *J. Phys. D Appl. Phys.* 4, 1589 (1971).
41. J. Lin, S. Banerjee, J. Lee, and C. Teng, *IEEE Electron Device Lett.* 11, 191 (1990).
42. V. Rajagopal Reddy, V. Janardhanam, J.W. Ju, H. Hong, and C.J. Choi, *Semicond. Sci. Technol.* 29, 075001 (2014).
43. A.C. Varghes and C.S. Menon, *Eur. Phys. J. B* 47, 485 (2005).
44. V. Rajagopal Reddy, *Appl. Phys. A* 116, 1379 (2014).

Publisher's Note Springer Nature remains neutral with regard to jurisdictional claims in published maps and institutional affiliations.